Supporting Information for:

Unraveling the Ground State and Excited State Structures and Dynamics of Hydrated Ce^{3+} Ions by Experiment and Theory

Patric Lindqvist-Reis,*† Florent Réal,*‡ Rafał Janicki‖, and Valérie Vallet,*‡

† Institute for Nuclear Waste Disposal, Karlsruhe Institute of Technology, P.O. Box 3640, 76021 Karlsruhe, Germany

‡ Univ. Lille, CNRS, UMR 8523 - PhLAM - Physique des Lasers Atomes et Molécules, F-59000 Lille, France

‖ University of Wrocław, Faculty of Chemistry, F. Joliot-Curie 14, 50-383 Wrocław, Poland

Table of Contents

1. Methods

1.1. Sample Preparation

1.1.1. Chemicals. $CeCl_3 \cdot 7H_2O$ (99.99 % Sigma-Aldrich), $LaCl_3 \cdot 7H_2O$ (99.99 % Sigma-Aldrich), $YCl_3 \cdot 6H_2O$ (99.99 % Sigma-Aldrich), La_2O_3 (99.99 %, Alfa Asear), $Ba(BrO_3)_2$ (Sigma-Aldrich), HCl (37%, puriss. p.a., Sigma-Aldrich), $HClO_4$ 70% (70.0-72.0%, puriss. p.a., Sigma-Aldrich), H_2SO_4 (puriss. p.a., 95-97%, Merck), HCF_3SO_3 (100 % Sigma-Aldrich), 15-crown-5 (98%, Sigma-Aldrich).

1.1.2. Solutions. A stock solution of 0.1 M $CeCl_3$ in 0.1 M HCl was prepared by dissolving weighted amounts of crystalline $CeCl_3 \cdot 7H_2O$ (99.99 %; Sigma-Aldrich) in 1 M HCl and dilution with water to 0.1 M. Aliquots of this stock solution were used to produce the more diluted aqueous Ce(III) solutions or to 'spike' the crystalline model compounds with Ce^{3+}.

1.1.3. Solids: **[La(H$_2$O)$_9$](BrO$_3$)$_3$ (1)**. An acidified (pH ~1) 0.5 M La$_2$(SO$_4$)$_3$ aqueous solution was obtained by dissolving La$_2$O$_3$ in H$_2$SO$_4$. Equimolar amounts of this solution and a Ba(BrO$_3$)$_2$ solution were mixed under stirring. The produced BaSO$_4$ precipitate was filtered off to give a clear solution. Several aliquots of this solution were spiked with CeCl$_3$ to give Ce:La molar ratios between 0.01 and 0.001%. Hexagonal rod-like crystals of **1** were formed from these solutions upon slow dehydration at room temperature.

[La(H$_2$O)$_9$](CF$_3$SO$_3$]$_3$ (2). An acidified (pH ~1) 0.2 M La(CF$_3$SO$_3$)$_3$ aqueous solution was obtained by dropwise addition of concentrated HCF$_3$SO$_3$ (100%; Sigma-Aldrich) to a slurry of La$_2$O$_3$ in water until the solution becomes clear. The solution was filtered to remove undissolved lanthanum oxide particles (if present). Aliquots of this solution were spiked with the Ce^{3+} stock solution to give Ce:La molar ratios between 0.01 and 0.001. Hexagonal rod-like crystals of **2** were grown from these solutions upon slow dehydration at room temperature.

[La(H$_2$O)$_7$Cl$_2$])$_2$Cl$_2$ (3). 0.40 g (1.08 mmol) LaCl$_3$·7H$_2$O (i.e. [La(H$_2$O)$_7$Cl$_2$])$_2$Cl$_2$) was dissolved in 0.1 M HCl and spiked with the cerium stock solution. Slow evaporation at room temperature yielded Ce^{3+}-doped crystals of **3**.

Y(H$_2$O)$_8$]Cl$_3$·15-crown-5 (4). 0.40 g (1.32 mmol) YCl$_3$·6H$_2$O was dissolved in 15 ml CH$_3$CN:CH$_3$OH 3:1. The solution was spiked with the cerium stock solution and heated to 60 °C. 0.29 g 1.32 mmol 15-crown-5 was dissolved in 5 ml CH$_3$CN:CH$_3$OH 3:1. This solution was added dropwise to the YCl$_3$ solution. The clear solution was covered and placed in the freezer. After ca. 2-3 days, colorless, plate-like crystals of **4** had formed.

[Ce(H$_2$O)$_7$Cl]Cl$_2$·15-crown-5·H$_2$O (5). The procedure is similar to that of **4**. 0.40 g (1.07 mmol) CeCl$_3$·7H$_2$O was dissolved in 15 ml CH$_3$CN:CH$_3$OH 3:1. The solution was spiked with the cerium stock solution and heated to 60 °C. 0.24 g 1.07 mmol 15-crown-5 was dissolved in 5 ml CH$_3$CN:CH$_3$OH 3:1. This solution was added dropwise to the YCl$_3$ solution. The clear solution was covered and placed in the freezer. After ca. 2-3 days, colorless, plate-like crystals had formed.

[Y(H$_2$O)$_6$Cl$_2$]Cl (6). 0.40 g (1.32 mmol) YCl$_3$·6H$_2$O (i.e. [Y(H$_2$O)$_6$Cl]Cl) was dissolved in 0.1 M HCl and spiked with the cerium(III) stock solution. Slow evaporation at room temperature yielded Ce^{3+}-doped crystals of **6**.

1.2. Crystallography

1.2.1. Single Crystal X-ray Diffraction. The crystal systems and the unit cell dimensions of the produced crystalline model compounds **1**-**4** and **6** were checked by single crystal X-ray diffraction methods with a Kuma KM4 diffractometer; they were found to be in agreement with the reported structures.[1] A single crystal of **5** of suitable size was cut from a larger crystal and mounted on a Kuma KM4 diffractometer equipped with a CCD counter. Data were corrected for polarization, Lorentz, and absorption (calculated from the crystal habit derived from photo scans). The position of the cerium atom was located from Patterson maps; all other atoms but hydrogen were derived from difference Fourier maps. The positions of all carbon-bonded hydrogen atoms were calculated geometrically. The refinement was done on the full-matrix with all of non-hydrogen atoms described anisotropically using the SHELXS97 and SHELXL-2018/1 programs.[2] The molecular structures depicted in Figure 1 and Figure S1 are drawn using the program DIAMOND 2.1, Crystal Impact GbR, 2001.

1.3. UV-vis Absorption Spectroscopy

Absorption spectra of the solids and the solutions were recorded with a Cary 5000 UV-Vis-NIR spectrophotometer. The solutions were measured in a 1 cm quartz cuvette at defined temperatures between 10-90 °C, controlled by a TC 125 in TLC 50 E temperature control unit. Compounds **2** and **4** were also measured at liquid helium temperature using an Oxford cryostat.

1.4. Time-Resolved Laser Fluorescence Spectroscopy (TRLFS)

TRLFS was performed using the fourth harmonic 266 nm of a Nd-YAG (Continuum Minilite Laser) laser system with a repetition rate of 10 Hz. The laser energy was about 1 mJ. Emission spectra were recorded in the range 290-440 nm. After spectral decomposition by a spectrograph (Shamrock 303i) with a 400 lines mm^{-1} grating the spectra were recorded using an ICCD camera (iStar Gen III, ANDOR) containing an integrated delay controller. The gate delay was 10 ns and the gate width 1000 ns. For luminescence lifetime the delay time was scanned with an interval of 6 ns. The lifetime τ was obtained by fitting the integrated intensity (I) at time t after the pulse to $I(\lambda) = I_0(\lambda) \exp(-t/\tau)$, where I_0 is the intensity at $t = 0$. In all the samples the emission decays were monoexponential (Figure S7).

1.5. Fluorescence Excitation Spectra

Fluorescence excitation spectra were obtained with the aid of an AB2 Aminco-Bowman Series 2 luminescence spectrometer equipped with a 7 W xenon lamp. The samples were contained in 1 cm quartz cuvettes.

1.6. Quantum Chemical Methods

1.6.1. Geometries of the Model Structures for the Quantum Chemical Calculations. To compute the vertical excitation energies of Ce^{3+} aqua species in different local hydration environments the following molecules species were constructed: $[Ce(H_2O)_8]^{3+}$, $[Ce(H_2O)_9]^{3+}$, $[Ce(H_2O)_9]^{3+}\cdot(H_2O)_{18}$, $[Ce(H_2O)_6Cl_2]^{+}$, $[Ce(H_2O)_7Cl]^{2+}$, and $[Ce(H_2O)_7Cl_2]^{+}$. The geometries corresponding to the models **1a,b,c-6a,b,c** are taken from the 'neat' crystal structures of **1-6** and either scaled to obtain a near-equilibrium structure of the doped Ce^{3+} ion (**1a-6a**), expanded (**1b-6b**), or reduced (**1c-6c**) in size. The near-equilibrium structures are obtained by scaling according to the difference in ionic radii between the host metal ion, La^{3+} or Y^{3+}, and Ce^{3+}. The purpose of the expanded and reduced structures is to study the influence of the cerium-ligand bond distances on the computed absorption spectra.

To optimize the geometries of the lowest excited $5d^1$ electronic states of the nonaaqua ion $[Ce(H_2O)_9]^{3+}$ time-dependent density functional theory (TD-DFT) calculations with the PBE0 functional[3] and excited states gradient calculations[4] have been performed using the parallel resolution of the identity approximation for the Coulomb,[5] with the appropriate atomic auxiliary basis functions.[6,7] The PBE0 functional was found to be accurate enough to reproduce the multi-state CASPT2 (complete active space perturbation theory at 2nd order),[8-10] MS-CASPT2 $4f^1$-$5d^1$ electronic absorption transition energies of the $[Ce(H_2O)_9]^{3+}$ ion (see

Table S18) and preventing ligand-to-metal charge-transfer transitions to spuriously occur in the $5d^1$ excited states manifold (neither did it occur in the wave-function calculations). In these calculations, the cerium atom was described by a small-core relativistic pseudopotential[11] with the corresponding def2-TZVP basis set.[12] All oxygen and hydrogen atoms, and chlorine ions were described with aug-cc-pVTZ basis sets.[13,14] The calculations were performed with the TURBOMOLE 7.1 quantum chemistry package.[15]

1.6.2. Electronic spectra calculations. For the calculations of spectra, the oxygen, hydrogen and chlorine basis sets are unchanged, but an all-electron atomic natural orbitals relativistic core correlation basis sets (ANO-RCC) with (25s22p15d11f4g) primitive functions contracted to quadruple-quality size [9s8p5d4f3g], was used to describe cerium. Scalar relativity was included through the second-order Douglas-Kroll-Hess Hamiltonian.[16] The wave-functions and energies of the 12 states corresponding to the $4f^1$ and $5d^1$ manifolds were obtained from state-averaged CASSCF (complete active space self-consistent field), with inclusion of dynamical electron correlation by MS-CASPT2 together with the ionization potential electron affinity (IPEA) corrected zeroth-order Hamiltonian.[17] The active space corresponds to distributing one electron in the seven 4*f* and five *5d* and the *6s* cerium orbital. In the MP2 and MS-CASPT2 calculations, the 1*s* core orbitals of the oxygen atoms, and core orbitals of the cerium ion were kept frozen. Spin-orbit coupling was treated by state interactions between the MS-CASPT2 wave functions, using the RASSI (restricted active space state interaction) program.[18] The SO operator matrix was calculated from atomic mean-field (AMFI) SO integrals.[19,20] All multi-reference CASPT2 and SO-CASPT2 calculations were run with the MOLCAS8.2 quantum chemistry package.[21] To identify the influence of the second and third coordination shells on the Ce^{3+} 4f and 5d electronic levels. If the effect of these long-range interactions is negligible on the spectra, we can simplify the model to consist of a discrete first coordination sphere along with a polarizable continuum model (PCM) mimicking water as a dielectric medium of permittivity of 78.39.[22,23] To find out, a set of four different calculations were carried out at the spin-free CASSCF level; the results are listed in Table S17. In the simplest model 4f-4f and 4f-5d transition energies were calculated for $[Ce(H_2O)_9]^{3+}$ in the gas phase. Extending this model with a PCM resulted in a small shift of ~30 cm^{-1} for the 4f-4f transitions and a slightly larger shift of ~100 cm^{-1} for the 4f-5d transitions. Interestingly, the addition of an explicit second hydration shell comprising 18 water molecules does not significantly change the 4f and 5d energy levels. Thus, a model consisting of a discrete first coordination shell combined with a PCM is sufficient for our purpose. This model reproduces rather well the Ce^{3+} 4f-5d optical spectra in the different host structures and in aqueous solution.

1.6.3. QTAIM analysis. To analyze the nature of the cerium-water/cerium-chloride chemical bond the quantum theory of atoms-in-molecules (QTAIM) analysis, we used the Gaussian 09 (Revision C01) quantum chemistry package,[24] with the same basis sets as to the Turbomole PBE0, which provides the appropriate wave-function extended files (wfx) to be used by the AIMAll package.[25] Note that the PBE0 functional was used to compute the density of the considered complexes.

2. Supporting Information for the Results and Discussion Section

2.1. Absorption Spectra

2.1.1. Absorption Spectra of 2 and 4 at 295 and 4 K. Figure S2 compares the room temperature and low temperature (4.2.K) spectra of Ce^{3+} in $[La(H_2O)_9](CF_3SO_3]_3$ (**2**) and $Y(H_2O)_8]Cl_3 \cdot$15-crown-5 (**4**).

2.1.2. Absorption vs. Excitation Spectra. Figure S3 (left) compares the absorption and fluorescence excitation (λ_{em} = 332 nm) spectra of the 4f-5d transitions of $[Ce_xLa_{1-x}(H_2O)_9](CF_3SO_3]_3$ (**2**) for x = 0.001 at room temperature. The positions and the widths of the five 5d bands are very similar in the two spectra, but the band intensity is reduced with increasing energy in the excitation spectrum. This is likely due to very short lifetimes of the higher energy states, affecting the energy transfer from these higher states to the lowest $5d^1$ energy level, which is the luminescent state. (Right) The effect of Ce^{3+} concentration on the fluorescence excitation spectra of **2** for x = 0.001, 0.01, 0.10, 0.50, and 1.0 at room temperature. As the concentration ratio increases the band widths of the five 5d states increases and band positions shift to longer wavelengths.

2.1.3. Thermodynamics of the Hydration Equilibrium. $4f^1 \rightarrow 5d^1$ absorption spectra of a Ce^{3+} aqueous solution (1.80 mM $CeCl_3$ in 20 mM HCl) were measured at temperatures between 10-90 °C in order to derive thermodynamic quantities for eq. 1. The spectra are shown in Figure 3a in the paper.

$$[M(H_2O)_9]^{3+} \rightleftharpoons [M(H_2O)_8]^{3+} + H_2O \quad (1)$$

The spectral changes with increasing temperature are rather small; however, they are most likely due to a change in the equilibrium between $[Ce(H_2O)_9]^{3+}$ and $[Ce(H_2O)_8]^{3+}$ species as of eq 1. The spectra are consistent with that the $[Ce(H_2O)_9]^{3+}$ ion is the main species also at 90 °C. The small but significant increase of the 295 nm band indicates that the concentration of $[Ce(H_2O)_8]^{3+}$ increases with temperature while that of $[Ce(H_2O)_9]^{3+}$ decreases (see Figure 3b in the main paper). It is not possible to obtain the spectra of individual species, hindering quantitative analysis of solution as a function of temperature. To elucidate this problem the spectra of the Ce^{3+}-doped crystals of **2** and **4** were used for deriving the molar fraction of the $[Ce(H_2O)_9]^{3+}$ and $[Ce(H_2O)_8]^{3+}$ species in solution. Neither could we determine the absolute intensities of the f-d transitions from the spectra of **2** and **4** since they were not of sufficiently high spectroscopic quality. Nevertheless, the relative intensities of the individual components of the f-d transitions derived from their absorption spectra enabled us to obtain the molar fractions of the octa- and nonahydrated Ce^{3+} species in solution. It is clearly seen in the spectra of the solutions that only the band centered at 296.6 nm may be attributed to the $[Ce(H_2O)_8]^{3+}$ species (see Figure S4 below and Figure 3a in the main paper). Consequently, only the changes of molar absorptivity coefficient of this band (hereinafter referred to as $\varepsilon_{296.6}$) may indicate the changes in the molar fraction of the $[Ce(H_2O)_8]^{3+}$ species. The band centered at 254.5 nm is ascribed mainly to the $[Ce(H_2O)_9]^{3+}$ species; however, this band is a superposition of 4f-5d transitions of both $[Ce(H_2O)_9]^{3+}$ and $[Ce(H_2O)_8]^{3+}$ species. Based on the spectrum of **4** we may assume that for the aqueous $[Ce(H_2O)_8]^{3+}$ species the relative ratio of $\frac{\varepsilon^8_{296.6}}{\varepsilon^8_{254.4}}$ = 1 for the bands centered at 296.6 and 254.5 nm, respectively. The determined $\Delta\varepsilon$ value at room temperature enabled us to conclude that the $\frac{\Delta\varepsilon^S_{254.5}}{\Delta\varepsilon^S_{296.6}}$ ratio is ~5.33, which may be

an indication that the ratios $\frac{\Delta\varepsilon^{S}_{254.5}}{\Delta\varepsilon^{S}_{296.6}}$ and $\frac{\varepsilon^{9}_{254.5}}{\varepsilon^{8}_{296.6}}$ should be very similar. Combining the equations 2-6 it was possible to calculate the molar fractions of both solution species as follows

$$\chi_8 \cdot \varepsilon^{8}_{254.5} + \chi_9 \cdot \varepsilon^{9}_{254.5} = \varepsilon^{S}_{254.5} \quad (2)$$

$$\chi_8 \cdot \varepsilon^{8}_{296.6} = \varepsilon^{S}_{296.6} \quad (3)$$

where χ_8 and χ_9 are the mole fractions of the $[Ce(H_2O)_8]^{3+}$ and $[Ce(H_2O)_9]^{3+}$ species, respectively. Taking into account from the spectra of **4** that

$$\frac{\varepsilon^{8}_{296.6}}{\varepsilon^{8}_{254.5}} = B = 0.958 \quad (4)$$

where B is the ratio of molar absorptivity coefficients for the respective bands for the $[Ce(H_2O)_8]^{3+}$ species, the molar fraction χ_9 may be calculated from equations 5 and 6.

$$\chi_9 = \frac{\varepsilon^{S}_{254.5} \cdot B - \varepsilon^{S}_{296.6}}{B \cdot \varepsilon^{9}_{254.5}} = Y_1 \quad (5)$$

$$\chi_9 = 1 - \frac{\varepsilon^{S}_{296.6}}{\varepsilon^{8}_{296.6}} = Y_2 \quad (6)$$

Minimizing the sum $\Sigma(Y_1\text{-}Y_2)^2$ it is possible to calculate $\varepsilon^{9}_{296.6}$, $\varepsilon^{8}_{296.6}$ and $\varepsilon^{8}_{254.4}$ for the $[Ce(H_2O)_8]^{3+}$ and $[Ce(H_2O)_9]^{3+}$ species. We obtained $\frac{\varepsilon^{9}_{254.5}}{\varepsilon^{8}_{296.6}} \approx 5.9$, which is consistent with $\frac{\Delta\varepsilon^{S}_{254.5}}{\Delta\varepsilon^{S}_{296.6}} \approx 5.3$. These results indicate that the intensity of the f-d transition of the $[Ce(H_2O)_8]^{3+}$ species in solution is about 6 times smaller as compared to the transitions of the aqueous $[Ce(H_2O)_9]^{3+}$ species. The quantum chemical calculations presented below give an independent confirmation that the oscillator strength of the $[Ce(H_2O)_9]^{3+}$ ion is noticeably larger than that of the $[Ce(H_2O)_8]^{3+}$ ion due to differences in the transition probabilities (cf. Tables S8 and S10), which are extremely sensitive to the local symmetry. Interestingly, at room temperature the concentration of the aqueous $[Ce(H_2O)_8]^{3+}$ ion is about sixteen percent relative to the aqueous $[Ce(H_2O)_9]^{3+}$ species in solution. Using the determined molar fractions of both isomers the equilibrium constant $K(T)$ of eq 1 could be calculated. By plotting $-\ln K$ versus T^{-1} (see Figure 3c in the main paper) and by applying the Van't Hoff equation

$$-\ln K = \Delta G^{o}/RT = \Delta H^{o}/RT - \Delta S^{o}/R \quad (7)$$

we obtained values for the enthalpy and entropy of the equilibrium reaction eq 1 in agreement with the values published earlier for Ce^{3+} and more recently for Cm^{3+} (see Table 1 in the main paper).[26,27]

2.1.4. Experimental Stokes Shift. Figure S5 compares the 4f-5d absorption and luminescence spectra of **2-5** and the aqueous Ce^{3+} solution at room temperature. Each absorption spectra is composed of five bands due to the transitions from the electronic $4f^1$ ground state to the five electronic levels of the excited $5d^1$ state, while the luminescence spectra are due to electronic transitions from the lowest $5d^1$ state to the lower lying $^2F_{5/2}$ and $^2F_{7/2}$ multiplets. This results in two broad contributions. These are fitted with Gaussian bands to account for the broadening caused by the electronic and vibronic transitions to the $^2F_{5/2}$ and $^2F_{7/2}$ crystal field levels. The splitting of the ^2F term into two $^2F_{5/2}$ and $^2F_{7/2}$ multiplets is due to spin-orbit interactions. The Stokes shift is defined as the difference in wavelength between the positions of the band maxima of absorption and emission spectra of the same electronic transition. In

all the measured absorption and emission spectra in present cerium(III) systems, the pure electronic transitions (zero-phonon lines) are not resolved from the vibronic transitions. If the zero-phonon lines coincide in absorption and emission spectra, this means that the structure of cerium(III) complex is not changed. Such is the situation for 4f-4f and 5f-5f transitions, which are well-shielded by the outer 5d and 6d orbitals, respectively. However, this is not the case for the Ce^{3+} $4f^1$-$5d^1$ transitions, which are subject of significant changes in the Ce^{3+} position as the photo-electron is excited into a $5d^1$ orbital with antibonding character. An extreme case the Ce^{3+} aqua ion, where photo-excitation results in a release of a water molecule, $[*Ce(H_2O)_9]^{3+} \rightarrow [*Ce(H_2O)_8]^{3+} + H_2O$, a process associated with a large change of the geometry of the $[*Ce(H_2O)_9]^{3+}$ complex in excited state and thus a large Stokes shift.

2.1.5. Luminescence Spectra and Lifetimes. The room temperature luminescence spectra of **2**-**5** and the aqueous Ce^{3+} solution are shown in Figure S6. Also shown in the figure is the low temperature (~4 K) spectrum of **2**. The room temperature spectra are curve-fitted with two Gaussian component bands to account for the electronic and vibronic contributions of the 5d-4f ($^2F_{5/2}$,$^2F_{7/2}$) transitions. The parity-allowed $5d^1$-$4f^1$ transition is associated with a relatively short luminescence lifetime in the nanosecond range. Because of the antibonding character of the 5d orbitals, a fast rearrangement takes place in the excited state. The rate constant for this process is much higher than the luminescence decay rate constant. This means that luminescence will mainly take place from the structurally "relaxed" species in the excited state, $[*Ce(H_2O)_8]^{3+}$. This can be depicted as follows: A $[*Ce(H_2O)_9]^{3+}$ species is excited to its $5d^1$ state. The structural instability of the excited state gives rise to a fast rearrangement to a $[*Ce(H_2O)_8]^{3+}$ species. Most of the luminescence takes place from $[*Ce(H_2O)_8]^{3+}$. Therefore, the derived luminescence lifetimes given in Table S5 are associated with $[*Ce(H_2O)_8]^{3+}$. As can be seen in Figure S7, the luminescence decays are all monoexponential.

2.1.6. Theoretical Structures. In order to gain confidence as to how sensitive the $4f^1$-$5d^1$ spectra are to the actual structure model, several different models were taken into consideration. Thus, we computed the $4f^1$-$5d^1$ absorption spectra of $[Ce(H_2O)_8]^{3+}$ in distorted bicapped trigonal prismatic (BTP) coordination geometries as well as in square antiprismatic geometries (SAP). In one of the BTP structures the Ce-O bond distances are 1.05 times longer than the Y-O distances in the crystal structure of **4**, compensating for the difference in ionic radii (in eight-coordination) between Y^{3+} (1.019 Å) and Ce^{3+} (1.143 Å). The mean Ce-O bond distance of this structure is 2.49 Å, which is a typical mean Ce-O bond distance for an eight-coordinated Ce^{3+} ion (cf. the Ce-O mean distance in **6**). In a second structure model with BTP geometry, the Ce-O bond distances equal the Y-O distances in **4**. Such large compression of the Ce-O distance due to the chemical pressure exerted on cerium in **4** is not realistic, however this structure model serves as a limiting case and is used to learn about how the spectrum change by changing the Ce-O distances. A similar study was performed with $[Ce(H_2O)_8]^{3+}$ ions in SAP geometries. Because of the similar ionic radii of Ce^{3+} and La^{3+}, the local structure of cerium in the doped lanthanum compounds are expected to be near to that of lanthanum. The minor differences in the metal-oxygen bond distances should be close to the differences in the ionic radii between the two metal ions. (see Table S1).

2.1.7. Theoretical Absorption Spectra. The calculated spectra for all the structures are reported in Tables S7-S11 and are also shown in Figure 6 and Figure S11. In Figure 6 in the main paper only the best calculated (**1a**-**6a**) spectra are shown together with the corresponding measured spectra. As can be seen in Figure 6 in the main paper the peak positions of the calculated spectra fit very well the peak maxima of the experimental spectra.

This indicates that the local structure of Ce^{3+} in the calculated structures is close to that of the real structures. Overall, the total crystal-field splitting of the $5d^1$ level is larger for shorter Ce-O bond distance. It is also larger for the eight-coordinate BTP geometry (**4**-**5**) than for the nine-coordinate TTP geometry for the same mean Ce-O distance (**1**-**3**). Moreover, for the eight-coordinate structures (**4**-**6**) the intensity of the high-wavelength band is rather pronounced in the experimental spectra but weak in the theoretical spectra, in particular for **6**. These results are compiled in Tables S7-S11 and displayed in Figure 6 and Figure S11.
Estimation of the Stokes-shifts is made by calculating the difference between the absorption energy from the lowest 4f state to the first 5d state at the ground-state geometry and the emission energy from the lowest 5d state to the 4f-manifold states at the lowest 5d optimized geometry.

2.1.8. About Tables S7-S12. These tables show the *ab initio* computed transition energies and of the $4f^1$-$4f^1$ and $4f^1$-$5d^1$ electronic transitions as well as oscillator strengths of $4f^1$-$5d^1$ electronic transitions for the Ce^{3+} in different coordination geometries corresponding to the crystal structures of the compounds **1**-**6**. The calculations were only including the atoms of the first coordination shell, for example $[Ce(H_2O)_9]^{3+}$ and $[Ce(H_2O)_7Cl]^{2+}$. All structures except the neat compound **5** are structures where Ce^{3+} ions replace the host metal ions. In these cerium-doped compounds, because the positions of the atoms in the first coordination sphere of cerium is not exactly known, we have assumed that cerium sits at the atomic position of the host metal ion and that the positions of the ligands are those of the host but scaled with a factor corresponding to the difference in the ionic radii between Ce^{3+} and the host metal ion. For several structures calculations were performed on expanded and contracted coordination geometries, where the atomic positions had been scaled accordingly from the assumed equilibrium positions. Due to the difference in ionic radii between Ce^{3+} and the host metal ion a certain degree of structural-mismatch appears in the vicinity of the cerium ion. Experimentally, it is difficult to determine the exact local structure (bond distances and bond angles) around the cerium dopant ion, although we may assume it is very similar to that of the replaced host metal ion. Thus in the isotypic $[Ln(H_2O)_9](CF_3SO_3)_3$ series the mean Ce-O bond distance of Ce^{3+} doped in $[La(H_2O)_9](CF_3SO_3)_3$ is assumed to be only marginally longer than the mean Ce-O bond distance in $[Ce(H_2O)_9](CF_3SO_3)_3$, but shorter than the mean La-O distance in the host structure.
In general, it is possible to derive fairly accurately the local structure around the dopant cerium ion with DFT calculations using periodic boundary conditions on large super cell structures of the host, in which one of the host metal ion is replaced by Ce^{3+}. However, this approach is out of scope for this paper as our aim is primarily to assess how the local structure influences the UV-vis absorption spectra and to some extent also the emission spectra of Ce^{3+} in doped compounds and in aqueous solution.

The labelling of the different models is as follows: model **1a-c**, model **2a-b**, model **3a**, model **4a-c**, model **5a**, and model **6a-c**. In the doped compounds the "**a**" structures correspond to an approximate "equilibrium" structure, in which the Ce-O bond distances are scaled according to the difference in the ionic radii between Ce^{3+} and the host metal ion; "**b**" structures correspond an expanded coordination shell, whereas the "**c**" structures correspond to a reduced coordination shell.

2.2. Figures (S1-S13)

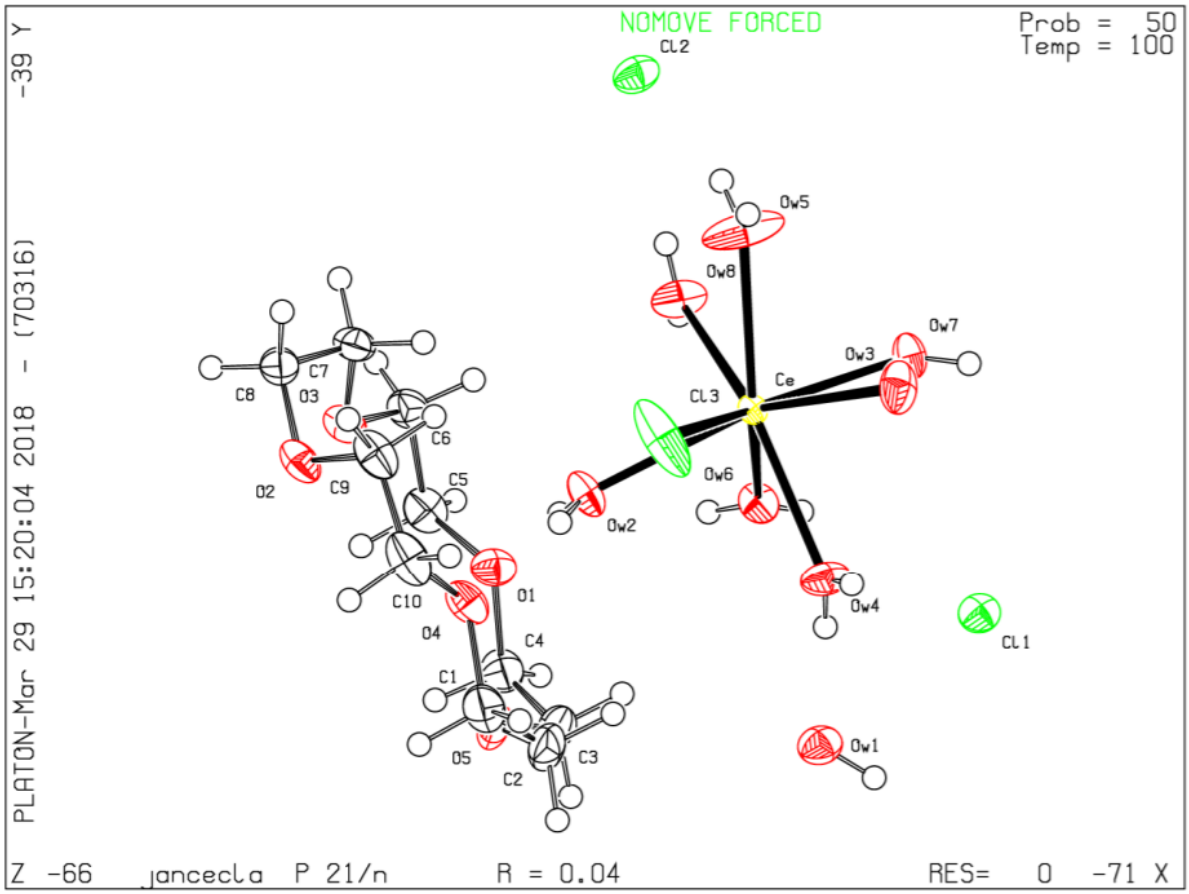

Figure S1. X-ray crystal structure of $[Ce(H_2O)_7Cl]Cl_2 \cdot 15\text{-crown-5} \cdot H_2O$ (**5**) at 100 K. Thermal ellipsoids are drawn at the 50% probability level. The Ce-O and Ce-Cl bond distances (in Å) are Ce-OW4 2.455(2); Ce-OW5 2.472(3); Ce-OW2 2.484(2); Ce-OW7 2.491(2); Ce-OW8 2.494(3); Ce-OW3 2.551(2); Ce-OW6 2.555(2); Ce-Cl3 2.7819(9).

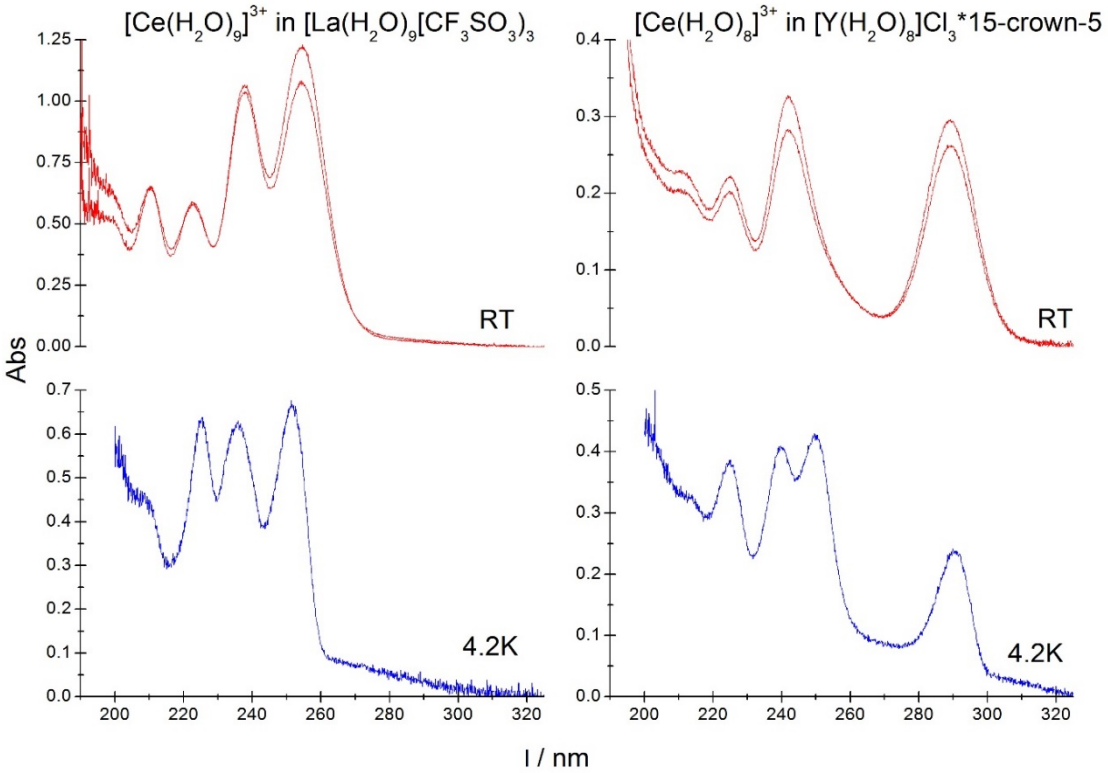

Figure S2. *Comparison of the room temperature and low temperature (4.2.K) spectra of* Ce^{3+} in $[La(H_2O)_9](CF_3SO_3]_3$ (**2**) and $Y(H_2O)_8]Cl_3 \cdot$15-crown-5 (**4**).

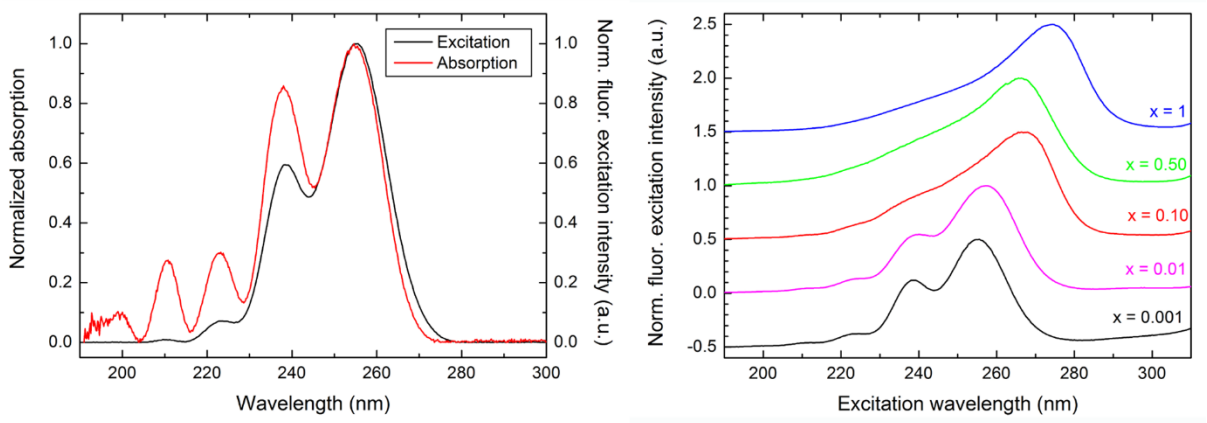

Figure S3. (Left) Absorption and fluorescence excitation (λ_{em} = 332 nm) spectra of the 4f-5d transitions of $[Ce_xLa_{1-x}(H_2O)_9](CF_3SO_3]_3$ (**2**) for x = 0.001 at room temperature. The positions and the widths of the five 5d bands are very similar in the two spectra, but the band intensity is reduced with increasing energy in the excitation spectrum. This is likely due to very short lifetimes of the higher energy states, affecting the energy transfer from these higher states to the lowest $5d^1$ energy level, which is the luminescent state. (Right) The effect of Ce^{3+} concentration on the fluorescence excitation spectra of **2** for x = 0.001, 0.01, 0.10, 0.50, and 1.0 at room temperature. As the concentration ratio increases the band widths of the five 5d states increases and band positions shift to longer wavelengths.

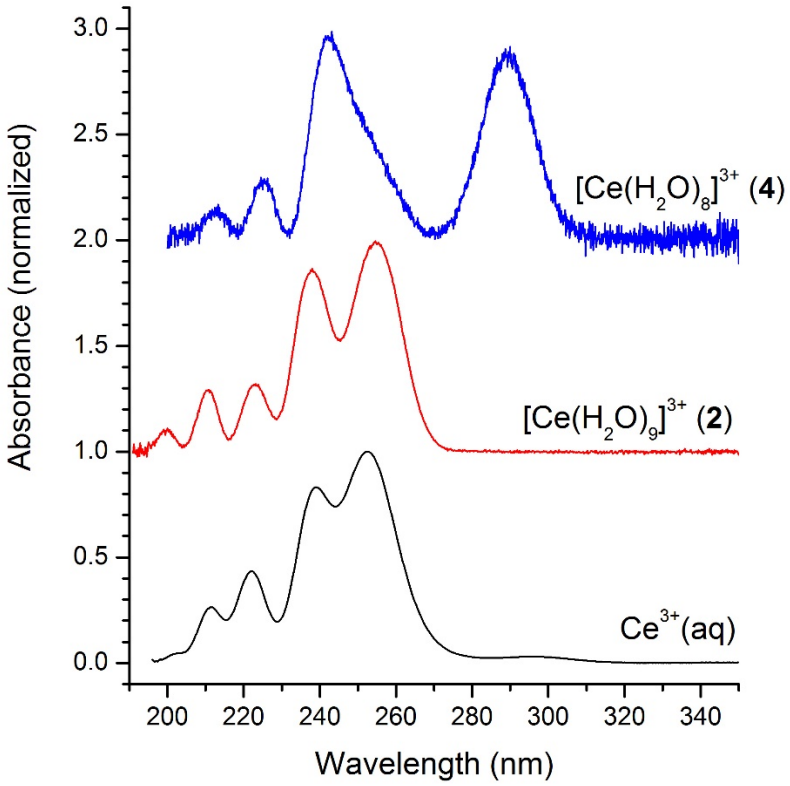

Figure S4. Comparison of the $4f^1 \rightarrow 5d^1$ room temperature absorption spectra of the aqueous cerium(III) solution (1.3 mM $CeCl_3$ in 0.01 M HCl) and Ce^{3+} in $[La(H_2O)_9](CF_3SO_3)_3$ (**2**) and $[Y(H_2O)_8]Cl_3 \cdot$15-crown-5 (**4**). The band maxima in the spectrum of **4** are bathochromically shifted in comparison with those recorded in the spectrum of **2**. This may indicate that the coordination number, i.e., the coordination geometry, is the main factor affecting the position of energy levels of $5d^1$ and $4f^1$ configurations. This nephelauxetic effect may indicate a weak covalent contribution to the Ce-O bond, which largely is ionic in nature. Thus, the bicapped trigonal prismatic geometry of the $[Ce(H_2O)_8]^{3+}$ cation in **4** with slightly shorter mean Ce-O bond distance compared to the regular tricapped trigonal prism geometry of the $[Ce(H_2O)_9]^{3+}$ cation in **2**, give rise to the redshifted bands seen in the spectrum of **4**. Observing such a redshift in aqueous solution may indicate a change in the coordination number.

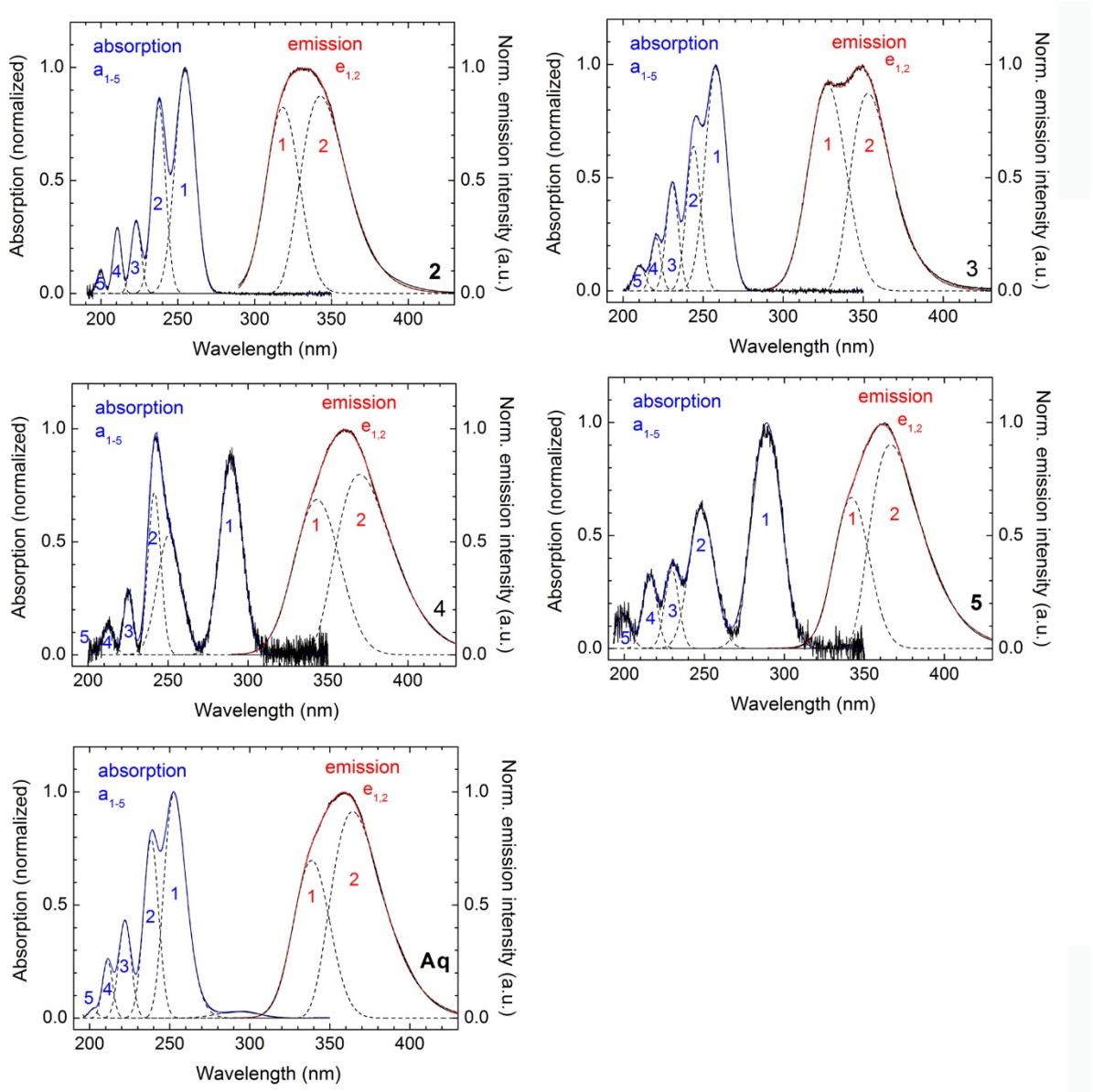

Figure S5. Comparison of the 4f-5d absorption and luminescence spectra of **2-5** and the aqueous Ce^{3+} solution at room temperature. Each absorption spectra is composed of five bands due to the transitions from the electronic $4f^1$ ground state to the five electronic levels of the excited $5d^1$ state, while the luminescence spectra are due to electronic transitions from the lowest $5d^1$ state to the lower lying $^2F_{5/2}$ and $^2F_{7/2}$ multiplets. This results in two broad contributions. These are fitted with Gaussian bands to account the temperature and vibronic line broadening of 4f-5d states. The splitting of the ^2F level is due to spin-orbit interactions.

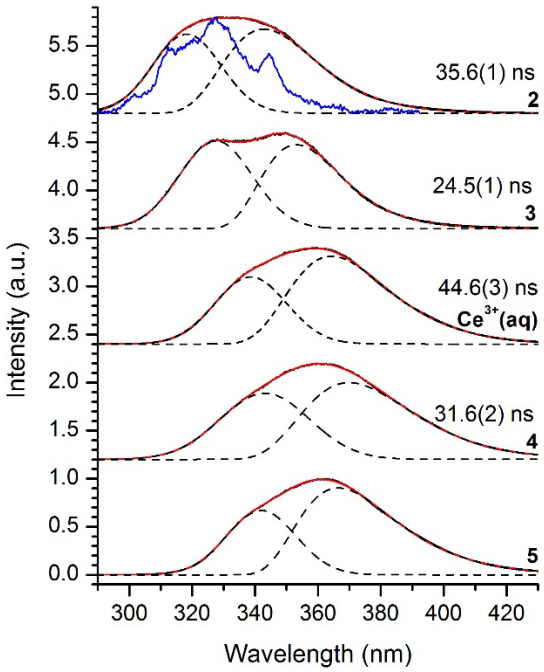

Figure S6. $5d^1 \rightarrow 4f^1$ luminescence spectra of Ce^{3+} in **2-5** and in aqueous solution (10^{-5} M Ce^{3+} in 0.01 M $HClO_4$) at room temperature. The spectra are fitted with two Gaussian bands, which account for the electronic and vibronic transitions to the $^2F_{5/2}$ and $^2F_{7/2}$ crystal field states, which are split due to the spin-orbit interaction. A luminescence spectrum of **2** at 4 K is also shown (blue line). Note that even at low temperature the (seven) zero phonon lines are not resolved due to vibronic broadening.

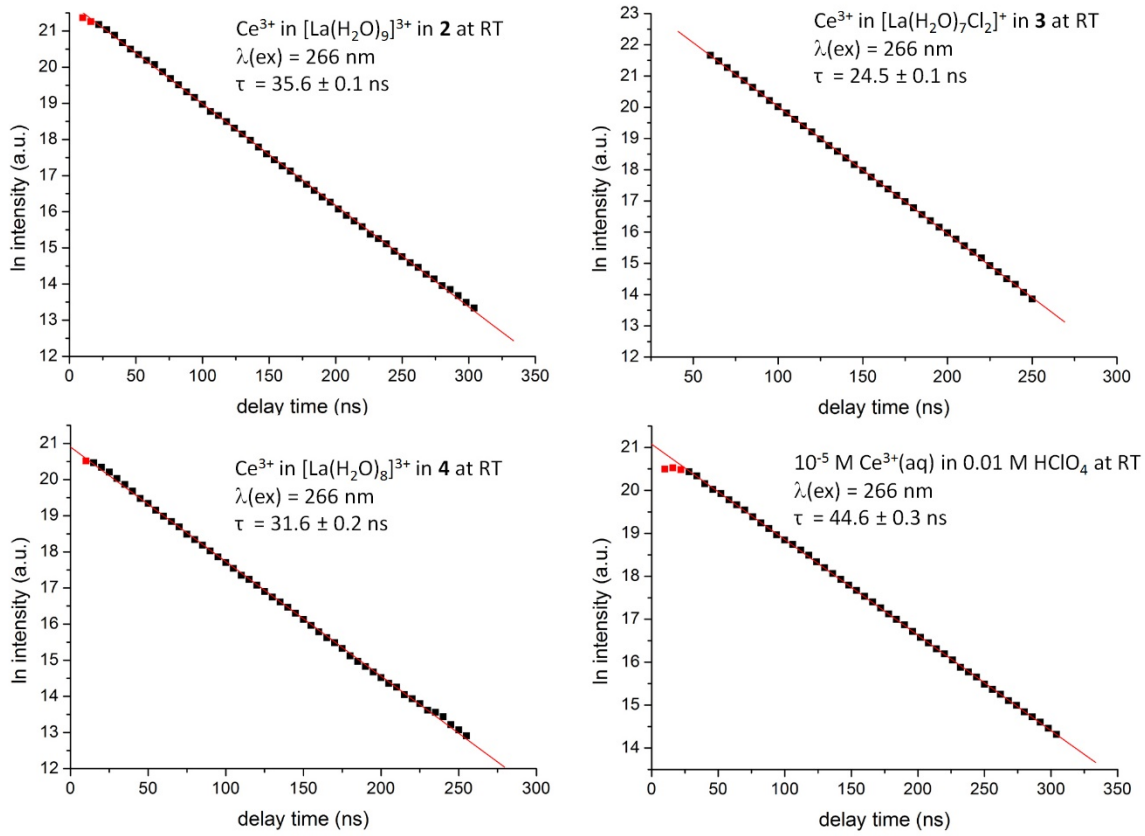

Figure S7. $5d^1 \rightarrow 4f^1$ luminescence decays (■) plotted on the logarithmic scale versus delay the time of Ce^{3+} in **2-5** and in aqueous solution (10^{-5} M Ce^{3+} in 0.01 M $HClO_4$) at room temperature. All the decays are monoexponential, which are fitted with straight line (red).

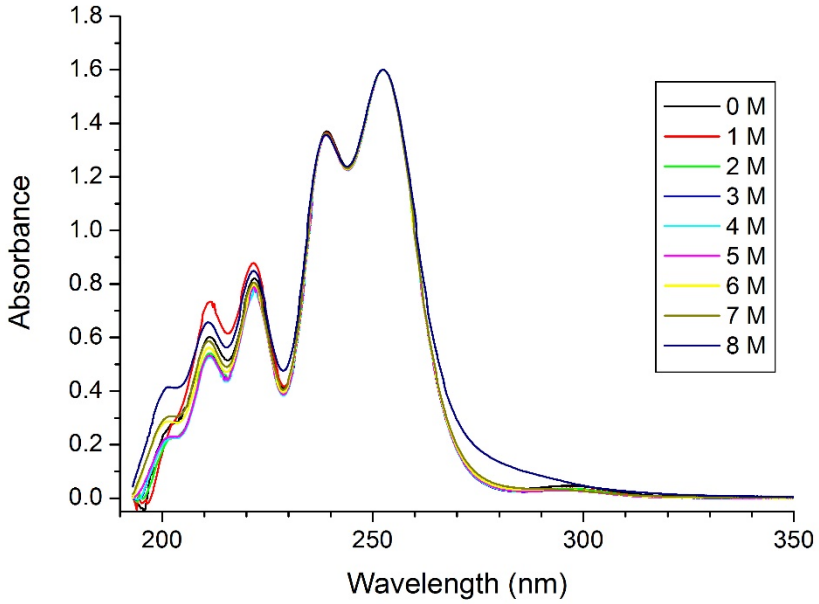

Figure S8. 4f-5d absorption spectra of 1.3 mM $Ce(ClO_4)_3$ in 0-8 M $NaClO_4$.

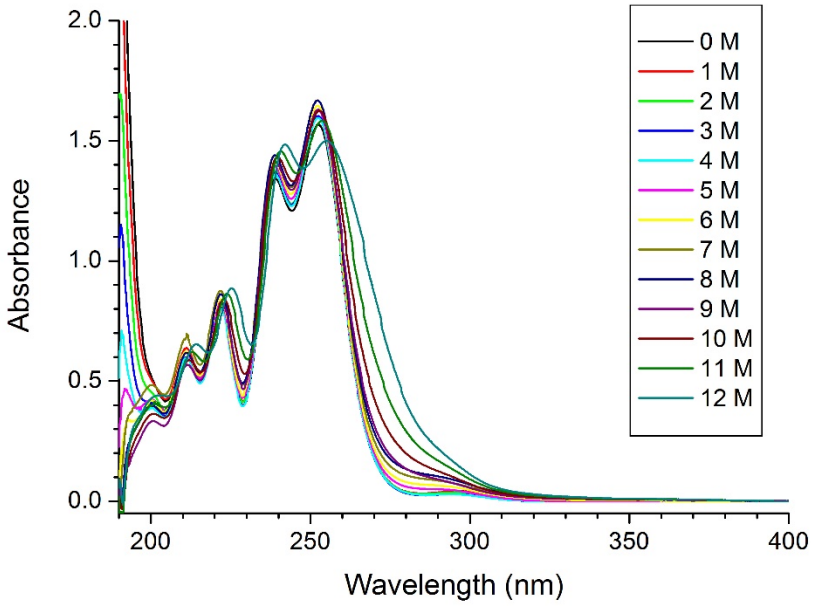

Figure S9. 4f-5d absorption spectra of 1.3 mM $Ce(ClO_4)_3$ in 0-12 M $HClO_4$.

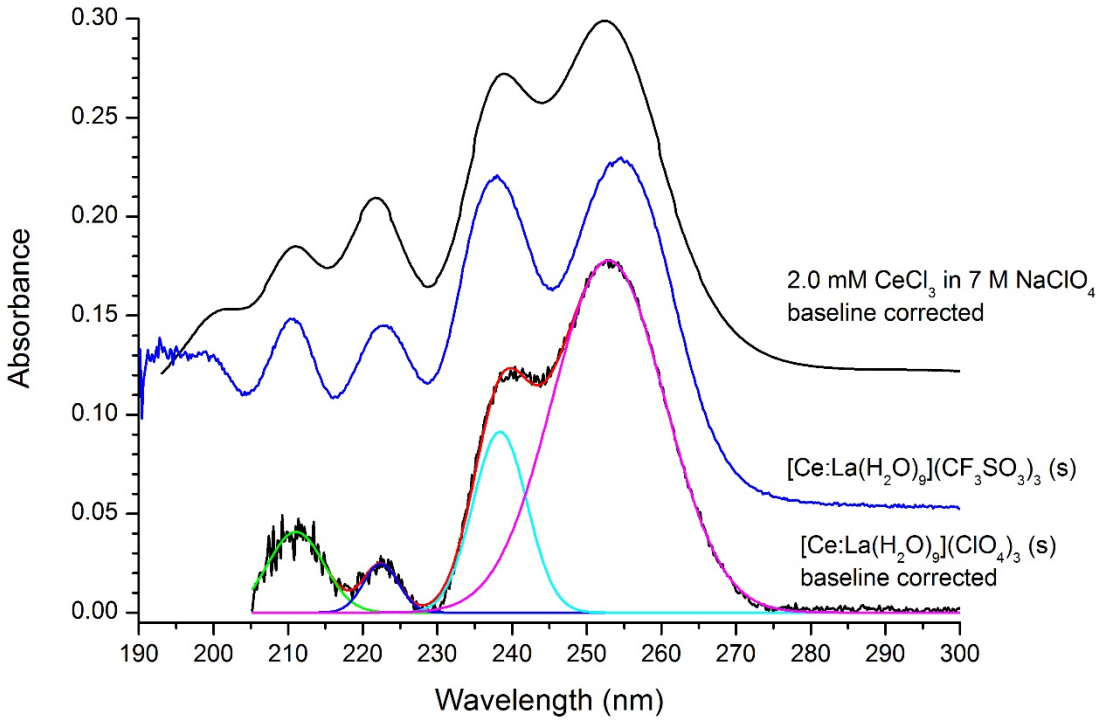

Figure S10. Comparison of 4f-5d absorption spectra of 1.3 mM $Ce(ClO_4)_3$ in 7 M $NaClO_4$, crystalline $[Ce:La(H_2O)_9](CF_3SO_3)_3$ and crystalline $[Ce:La(H_2O)_9](ClO_4)_3$ at room temperature.

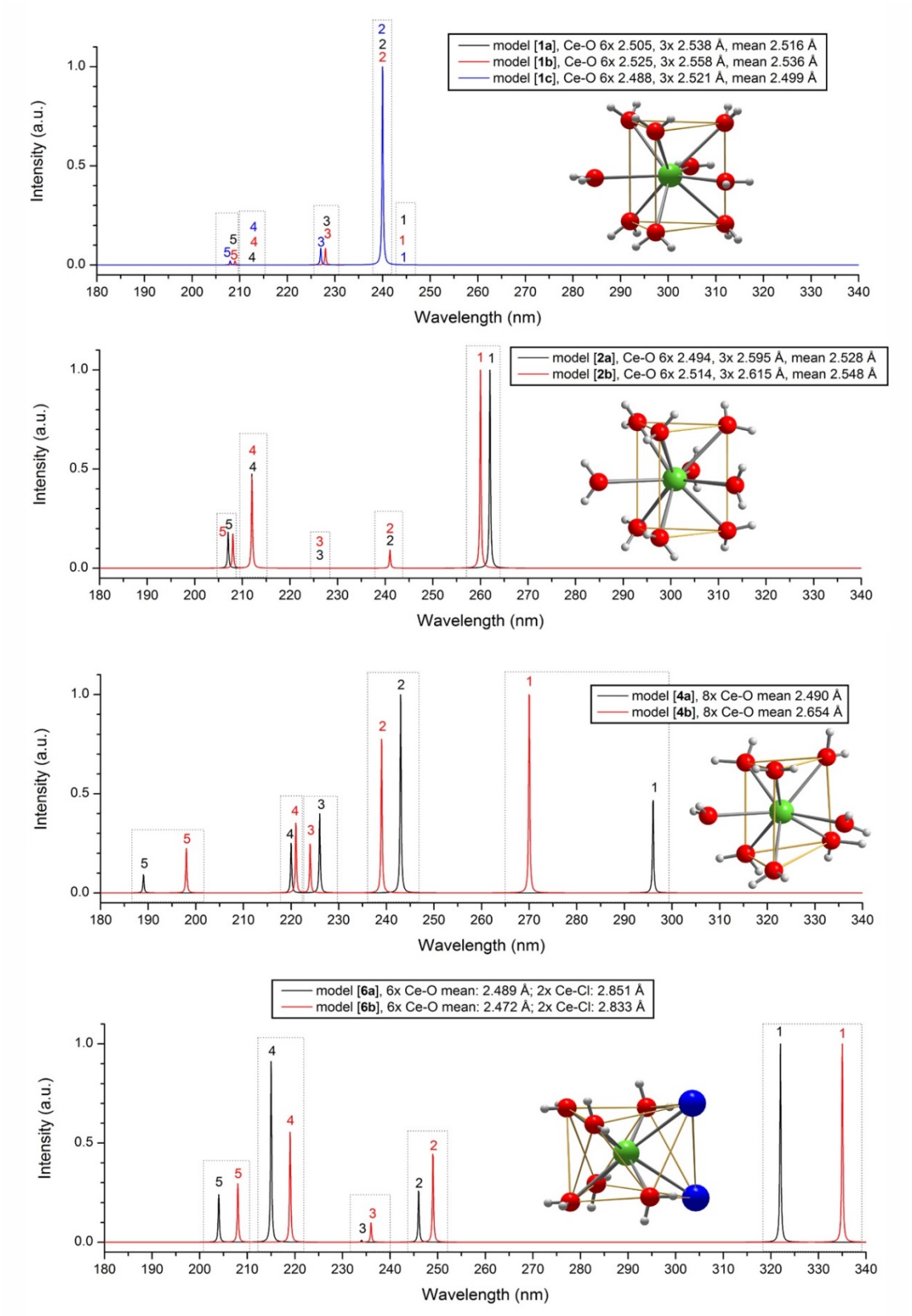

Figure S11. Computed absorption spectra for various coordination model around Ce^{3+} ion at the SO-CASPT2 level. Models are defined in Tables S7-S11.

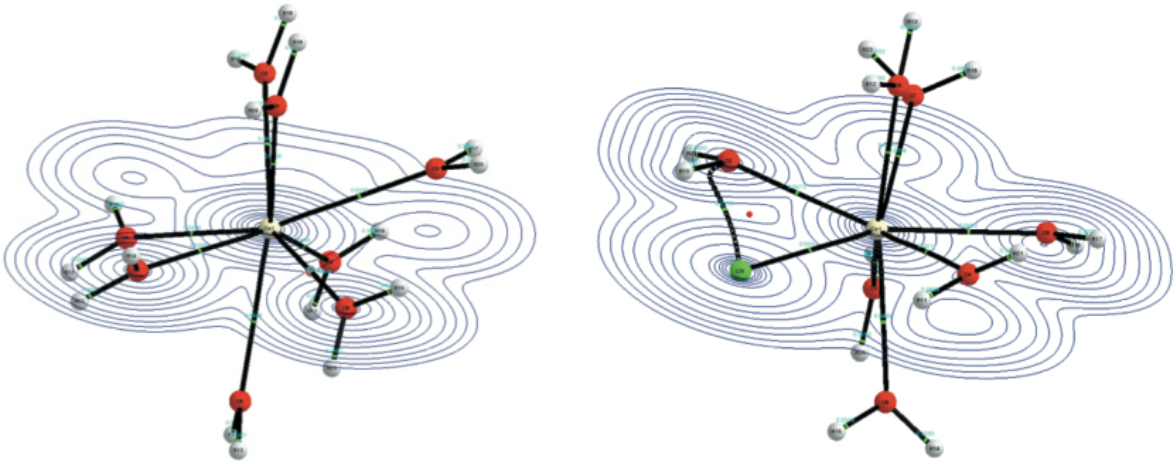

Figure S12. Electron densities of $[Ce(H_2O)_8]^{3+}$ and $[Ce(H_2O)_7Cl]^{2+}$. Contour maps of the electronic densities are shown as thin blue lines; the BCPs are shown as small green spheres.

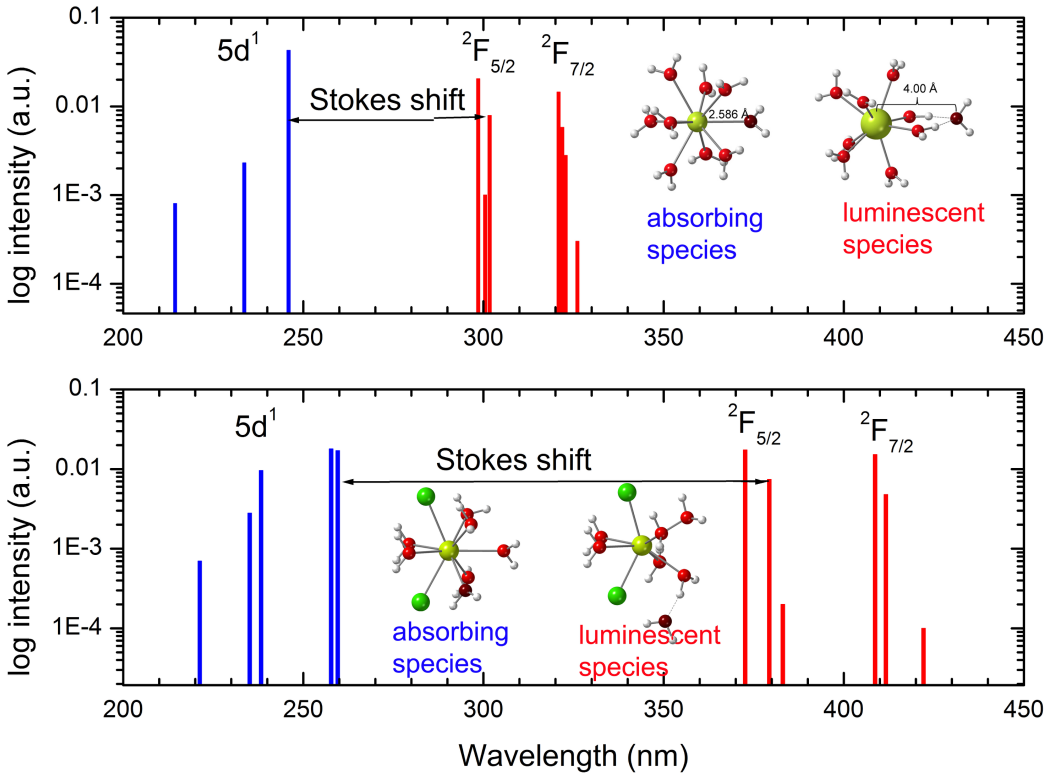

Figure S13. Computed absorption spectra of the $[Ce(H_2O)_9]^{3+}$ and the $[Ce(H_2O)_7Cl_2]^{+}$ species and the corresponding emission spectra of $[^*Ce(H_2O)_8]^{3+}\cdot H_2O$ and $[^*Ce(H_2O)_6Cl_2]\cdot H_2O$. The data are taken from Tables S15 and S16.

2.3. Tables (S1-S18)

Table S1: Coordination Geometry Data with Metal-Oxygen/Chloride Bond Distances [and Mean Distances] of the Ce-Doped Compounds (**1**-**4**, **6**) and the Neat Compound (**5**) and Estimated Ce-O and Ce-Cl Bond Distances for the Ce-Doped Compounds

host; coordination geometry (symm.) of metal ion	metal-oxygen and metal-chloride bond distances (Å)
1 $[La(H_2O)_9](BrO_3)_3$; TTP (D_{3h})	La-O 6×2.525, 3×2.558 [2.536][a]; Ce-O 6×2.51, 3×2.54 [
2 $[La(H_2O)_9](CF_3SO_3)_3$; TTP (C_{3h})	La-O 6×2.514, 3×2.615; [2.548]; Ce-O 6×2.49, 3×2.59 [
3 $[La(H_2O)_7(\mu\text{-}Cl)]_2Cl_4$; TTP ($C_1$)	La-O 2.529-2.586 [2.562]; La-Cl 2.924, 2.958 [2.941]; C 2.93 [2.91]
4 $[Y(H_2O)_8]Cl_3$·15-crown-5; BTP (~C_2)	Y-O 2.317-2.432 [2.366]; Ce-O 2.44-2.56 [2.49] [d]
5 $[Ce(H_2O)_7Cl]Cl_2$·15-crown-5·H_2O; BTP (~C_2)	Ce-O 2.455-2.556 [2.499]; Ce-Cl 2.782
6 $[Y(H_2O)_6Cl_2]Cl$; SAP (~C_2)	Y-O 2.334-2.361; [2.352]; Y-Cl 2×2.740; Ce-O 2.47-2.5

[a] The La-O and Ce-O distances of the $[La(H_2O)_9]^{3+}$ and $[Ce(H_2O)_9]^{3+}$ ions in **1** are assumed to be slightly longer than the Pr-O distances in $[Pr(H_2O)_9](BrO_3)_3$, 6×2.488 and 3×2.521 Å. Using the difference in ionic radii in nine-coordination between La^{3+} (1.216 Å) and Pr^{3+} (1.179 Å) and between Ce^{3+} (1.196 Å) and Pr^{3+} (1.179 Å) we estimate the La-O and Ce-O distances in **1** to be about 0.037 and 0.017 Å longer, respectively, than the reported distances in $[Pr(H_2O)_9](BrO_3)_3$. [b] The Ce-O distance of the $[Ce(H_2O)_9]^{3+}$ ions in **2** are assumed to be very close to the distances in $[Ce(H_2O)_9](CF_3SO_3)_3$. [c] The Ce-O and Ce-Cl distance of the $[Ce(H_2O)_7Cl_2]^+$ ions in **3** are assumed to be close to the distances in $[Ce(H_2O)_7(\mu\text{-}Cl)]_2Cl_4$. [d] The Ce-O distance of the $[Ce(H_2O)_8]^{3+}$ ions in **4** are assumed to be slightly longer than the Sm-O distances in $[Sm(H_2O)_8]Cl_3$·15-crown-5 (my own data). Using the ionic radii difference between Ce^{3+} and Sm^{3+} in eight-coordination, 1.143 and 1.079 Å, respectively, we estimate the Ce-O distance in **4** to be ca. 0.064 Å longer than those reported $[Sm(H_2O)_8]Cl_3$·15-crown-5 Å. The same results is obtained if we chose to compare with $[Y(H_2O)_8]Cl_3$·15-crown-5 (**4**) by adding 0.124. Å to the Y-O bond distances. [e] The Ce-O and Ce-Cl distance of the $[Ce(H_2O)_6Cl_2]^+$ ions in **6** are assumed to be close to the distances in $[Ce(H_2O)_6Cl_2]Cl$.

Table S2. Crystal Data of **5**.

$C_{10}H_{32}CeCl_3O_{13}$	$F(000) = 1220$
$M_r = 606.82$	$D_x = 1.693$ Mg m^{-3}
Monoclinic, $P2_1/n$	Mo $K\alpha$ radiation, $\lambda = 0.71073$ Å
$a = 10.831$ (2) Å	Cell parameters from 12669 reflections
$b = 16.236$ (2) Å	$\theta = 2.9$–$36.6°$
$c = 13.544$ (2) Å	$\mu = 2.30$ mm^{-1}
$\beta = 91.23$ (2)°	$T = 100$ K
$V = 2381.2$ (6) Å^3	Irregular, colorless
$Z = 4$	0.19 × 0.17 × 0.12 mm

Table S3: Data Collection of **5**.

Xcalibur, Sapphire2, large Be window diffractometer	5498 reflections with $I > 2\sigma(I)$
Radiation source: Enhance (Mo) X-ray Source	$R_{int} = 0.046$
Detector resolution: 8.3359 pixels mm^{-1}	$\theta_{max} = 36.7°$, $\theta_{min} = 2.9°$
Absorption correction: analytical *CrysAlis RED*, Oxford Diffraction Ltd., Version 1.171.33.66 (release 28-04-2010 CrysAlis171 .NET) (compiled Apr 28 2010,14:27:37) Analytical numeric absorption correction using a multifaceted crystal model based on expressions derived by R.C. Clark & J.S. Reid. (Clark, R. C. & Reid, J. S. (1995). Acta Cryst. A51, 887-897)	$h = -13 \rightarrow 14$
$T_{min} = 0.649$, $T_{max} = 1.000$	$k = -26 \rightarrow 21$
17189 measured reflections	$l = -13 \rightarrow 18$
6542 independent reflections	

Table S4: Refinement of **5**.

Refinement on F^2	0 restraints
Least-squares matrix: full	Hydrogen site location: mixed
$R[F^2 > 2\sigma(F^2)] = 0.038$	H atoms treated by a mixture of independent and constrained refinement
$wR(F^2) = 0.106$	$w = 1/[\sigma^2(F_o^2) + (0.0754P)^2]$ where $P = (F_o^2 + 2F_c^2)/3$
$S = 1.03$	$(\Delta/\sigma)_{max} = 0.001$
6542 reflections	$\Delta\rho_{max} = 1.27$ e Å^{-3}
296 parameters	$\Delta\rho_{min} = -0.78$ e Å^{-3}

Table S5: Peak maxima of the deconvoluted $4f^1$-$5d^1$ room temperature emission spectra in Figure 6 and the corresponding emission lifetime of Ce^{3+} in **2**, **3**, **4**, **5**, and in aqueous solution.

sample	λ_{em} band 1 (nm)	λ_{em} band 2 (nm)	Δ (cm^{-1})	τ (ns)
2	318	343	2240	35.6 ± 0.1
3	327	353	2240	24.5 ± 0.1
4	343	369	2050	31.6 ± 0.2
5	342	367	1990	-
10^{-5} M Ce^{3+}(aq)	339	364	2080	44.6 ± 0.3

Table S6: Lowest absorption band (emitting state), deconvoluted emission band (band 1, $^2F_{5/2}$) and Stokes shift of Ce^{3+} in **2**, **3**, **4**, **5**, and in aqueous solution (cf. Figure S5).

sample	λ_{abs} band 1 (nm)	λ_{em} band 1, $^2F_{5/2}$ (nm)	Stokes shift (cm^{-1})
2	255	318	7770
3	258	327	8180
4	289	343	5450
5	289	342	5390
10^{-5} M Ce^{3+}(aq)	253	339	10060

Table S7: Computed Ce^{3+} $4f^1$-$4f^1$ and $4f^1$-$5d^1$ Transition Energies (*E*), Transition Wavelengths (λ), and Oscillator Strengths (*f*) of $[Ce(H_2O)_9]^{3+}$ with Different Ce-O Bond Distances in Tricapped Trigonal Prismatic Geometry and D_{3h} Symmetry as in the Crystal Structures of $[La(H_2O)_9](BrO_3)_3$

	model **1a** equilibrium Ce-O distances 6×2.505, 3×2.538 Å (mean: 2.516 Å)			model **1b** expanded Ce-O distances 6×2.525, 3×2.558 Å, (mean 2.536 Å)			model **1c** reduced Ce-O distances 6×2.488, 3×2.521 Å, (mean 2.499 Å)		
transition	*E*, cm^{-1}	λ, nm	*f*, a.u.	*E*, cm^{-1}	λ, nm	*f*, a.u.	*E*, cm^{-1}	λ, nm	*f*, a.u.
$4f^1$-$4f^1$	0			0			0		
	184			147			204		
	224			191			237		
	2288			2278			2290		
	2461			2427			2478		
	2574			2545			2594		
	2607			2577			2635		
$4f^1$-$5d^1$	40614	246	0.0000	40680	246	0.0000	40397	248	0.0000
	41699	240	0.0429	41746	240	0.0428	41654	240	0.0428
	43895	228	0.0034	43950	228	0.0036	43845	227	0.0036
	47049	213	0.0000	46896	213	0.0000	47099	212	0.0000
	48006	209	0.0009	47850	209	0.0009	48062	208	0.0009

Table S8: Computed Ce^{3+} $4f^1$-$4f^1$ and $4f^1$-$5d^1$ Transition Energies (E), Transition Wavelengths (λ), and Oscillator Strengths (f) of $[Ce(H_2O)_9]^{3+}$ with Different Ce-O Bond Distances in Tricapped Trigonal Prismatic Geometry and C_{3h} Symmetry as in the Crystal Structures of $[La(H_2O)_9](CF_3SO_3)_3$

	model **2a** equilibrium Ce-O distances 6×2.494, 3×2.595 Å (mean 2.528 Å)			M = La, model **2b** expanded Ce-O distances 6×2.514, 3×2.615 Å (mean 2.548 Å)		
transition	E, cm^{-1}	λ, nm	f, a.u.	E, cm^{-1}	λ, nm	f, a.u.
$4f^1$-$4f^1$	0			0		
	67			58		
	209			200		
	2281			2282		
	2335			2329		
	2522			2512		
	2534			2525		
$4f^1$-$5d^1$	38237	262	0.0270	38478	260	0.0272
	41450	241	0.0024	41482	241	0.0025
	43606	229	0.0000	43645	229	0.0000
	47269	212	0.0126	47120	212	0.0123
	48290	207	0.0048	48134	208	0.0046

Table S9: Computed Ce^{3+} $4f^1$-$4f^1$ and $4f^1$-$5d^1$ Transition Energies (E), Transition Wavelengths (λ), and Oscillator Strengths (f) for $[Ce(H_2O)_7Cl_2]^+$ in $[Ce(H_2O)_7(\mu\text{-}Cl)]_2Cl_4$ and $[Ce(H_2O)_7Cl]^{2+}$ in $[Ce(H_2O)_7Cl]Cl_2 \cdot 15\text{-crown-}5 \cdot H_2O$

	model **3a** $[Ce(H_2O)_7Cl_2]^+$, equilibrium distances: Ce-O 2.494-2.554 Å (mean 2.523 Å) Ce-Cl 2.898, 2.926 Å (mean 2.912 Å)			model **5a** $[Ce(H_2O)_7Cl]^{2+}$, equilibrium distances: Ce-O 2.455-2.556 Å (mean 2.499 Å) Ce-Cl 2.782		
transition	E, cm^{-1}	λ, nm	f, a.u.	E, cm^{-1}	λ, nm	f, a.u.
$4f^1$-$4f^1$	0			0		
	66			167		
	289			393		
	2270			2303		
	2342			2386		
	2484			2524		
	2656			2827		
$4f^1$-$5d^1$	38601	259	0.0170	32412	309	0.0189
	38872	257	0.0179	39585	253	0.0065
	42053	238	0.0096	43416	230	0.0044
	42620	235	0.0028	45244	221	0.0077
	45294	221	0.0007	49758	201	0.0068

Table S10: Computed Ce^{3+} $4f^1$-$4f^1$ and $4f^1$-$5d^1$ Transition Energies (E), Transition Wavelengths (λ), and Oscillator Strengths (f) of $[Ce(H_2O)_8]^{3+}$ with Different Ce-O Bond Distances in Bicapped Trigonal Prismatic Geometry as in $[Y(H_2O)_8]Cl_3 \cdot$15-crown-5

	model **4a** equilibrium Ce-O distances range: 2.440-2.560 Å (mean 2.490 Å)			model **4b** expanded Ce-O distances range: 2.599-2.728 Å (mean 2.654 Å)			model **4c** reduced Ce-O distances range: 2.316- 2.432 Å. (mean: 2.366 Å)		
transition	E, cm^{-1}	λ, nm	f, a.u.	E, cm^{-1}	λ, nm	f, a.u.	E, cm^{-1}	λ, nm	f, a.u.
$4f^1$-$4f^1$	0			0			0		
	64			53			131		
	410			268			597		
	2258			2290			2225		
	2322			2343			2330		
	2539			2464			2688		
	2786			2642			2955		
$4f^1$-$5d^1$	33832	296	0.0098	37081	270	0.0174	30912	324	0.0041
	41132	243	0.0209	41944	239	0.0133	40412	248	0.0272
	44198	226	0.0083	44580	224	0.0042	44137	227	0.0118
	45445	220	0.0052	45253	221	0.0060	45928	218	0.0036
	52981	189	0.0019	50622	198	0.0038	55265	181	0.0013

Table S11: Computed Ce^{3+} $4f^1$-$4f^1$ and $4f^1$-$5d^1$ Transition Energies (E), Transition Wavelengths (λ), and Oscillator Strengths (f) of $[Ce(H_2O)_6Cl_2]^+$ with Different Ce-O Bond Distances in Near Square Antiprismatic Geometries as in the Isotypic $[Y(H_2O)_6Cl_2]Cl$ and $[Pr(H_2O)_6Cl_2]Cl$ Salts

	model **6a** equilibrium Ce-O distances 2×2.468, 2×2.496, 2×2.503 Å (mean 2.489 Å) Ce-Cl: 2×2.851 Å			model **6b** reduced Ce-O distances 2×2.451, 2×2.479, 2×2.486 Å (mean 2.472 Å) Ce-Cl: 2×2.833 Å			model **6c** reduced Ce-O distances 2×2.334, 2×2.360, 2×2.361 Å (mean 2.352 Å) Ce-Cl: 2×2.740 Å		
transition	E, cm^{-1}	λ, nm	f, a.u.	E, cm^{-1}	λ, nm	f, a.u.	E, cm^{-1}	λ, nm	f, a.u.
$4f^1$-$4f^1$	0			0			0		
	172			340			177		
	409			483			479		
	2259			2315			2225		
	2406			2480			2363		
	2600			2683			2708		
	2899			2941			3051		
$4f^1$-$5d^1$	31101	322	0.0184	29847	335	0.0180	27735	363	0.0164
	40627	246	0.0048	40210	249	0.0081	40232	249	0.0061
	42768	234	0.0002	42489	236	0.0018	42318	236	0.0005
	46584	215	0.0167	45664	219	0.0100	48071	208	0.0182
	49129	204	0.0044	48174	208	0.0053	50048	200	0.0048

Table S12: Computed Ce^{3+} $4f^1$-$4f^1$ and $4f^1$-$5d^1$ Transition Energies (E), Transition Wavelengths (λ), and Oscillator Strengths (f) for $[Ce(H_2O)_8]^{3+}$ with Square Antiprismatic (SAP) Geometry

	model **7a** SAP geometry Ce-O distances 2.490 × 8 Å			model **7b** SAP geometry Ce-O distances 2.538 × 8 Å			model **7c** perfect SAP geometry [a] Ce-O distances 2.551 × 8 Å		
transition	E, cm^{-1}	λ, nm	f, a.u.	E, cm^{-1}	λ, nm	f, a.u.	E, cm^{-1}	λ, nm	f, a.u.
$4f^1$-$4f^1$	0			0			0		
	283			275			72		
	387			342			191		
	2338			2349			2331		
	2476			2447			2338		
	2525			2530			2365		
	2895			2839			2568		
$4f^1$-$5d^1$	32138	311	0.0204	33353	300	0.0201	35592	281	0.0231
	41928	239	0.0029	42079	238	0.0028	41913	239	0.0028
	44067	227	0.0001	44222	226	0.0000	44076	227	0.0000
	47952	209	0.0175	47701	210	0.0174	46620	215	0.0155
	49119	204	0.0035	48798	205	0.0031	47697	210	0.0031

[a] The H atom positions are constrained to satisfied the SAP structure but O-H distances and H-O-H angles are optimized at the MP2 level.

Table S13: QTAIM charge (Q(M)) and the ratio d(Ce-BCP)/d(Ce-L), the electron density (ρ_b), Laplacian ($\nabla^2\rho_b$), and the energy density (H_b) at the An-X (Cl, O) bond critical point.

		Q(M)	d(Ce-BCP)/d(Ce-L) %	ρ_b [e^-/bohr^3]	$\nabla^2\rho_b$ [e^-/bohr^5]	H_b [a.u.]
$[Ce(H_2O)_9]^{3+}$	Ce-O_{capped}	2.43	50	0.037	0.146	0.0015
	Ce-O_{prism}			0.039	0.152	0.0011
$[*Ce(H_2O)_9]^{3+}$	Ce-O_{capped}	2.43	50	0.041	0.133	-0.0015
	Ce-O_{prism}			0.039	0.153	-0.0001
$[Ce(H_2O)_7Cl_2]^{+}$	Ce-Cl	2.28	50	0.046	0.103	0.0065
	Ce-O		54	0.039	0.151	-0.0008
$[Ce(H_2O)_8]^{3+}$	Ce-O	2.44	54	0.041	0.156	0.0004
$[Ce(H_2O)_7Cl]^{2+}$	Ce-Cl	2.33	50	0.049	0.104	-0.0083
	Ce-O		54	0.046	0.178	-0.0007

Table S14: Natural bond orbital (NBO) population and charge analysis for the ground-state (GS) and first excited state (ES) of Ce(III) aqua and aqua-chloro complexes. DFT and TD-DFT Calculations were performed using the PBE0 functional. The populations are expressed in electron units.

Complex	Excited state	Ce populations	Ce Charge
$[Ce(H_2O)_8]^{3+}$ (SAP)	GS	$6s^{0.12}4f^{1.07}5d^{0.60}6p^{0.24}5f^{0.04}6d^{0.02}$	1.91
$[*Ce(H_2O)_8]^{3+}$ (dist. SAP)	ES	$6s^{0.14}4f^{0.16}5d^{1.63}6p^{0.24}5f^{0.02}6d^{0.07}$	1.72
$[Ce(H_2O)_9]^{3+}$ (TTP)	GS	$6s^{0.14}4f^{1.08}5d^{0.70}6p^{0.30}5f^{0.05}6d^{0.02}$	1.72
$[*Ce(H_2O)_8]^{3+}\cdot H_2O$	ES	$6s^{0.15}4f^{0.38}5d^{1.64}6p^{0.31}5f^{0.06}6d^{0.11}$	1.33
$[Ce(H_2O)_7Cl_2]^{1+}$	GS	$6s^{0.18}4f^{1.10}5d^{1.01}6p^{0.43}5f^{0.07}6d^{0.04}$	1.17
$[*Ce(H_2O)_6Cl_2]\cdot H_2O$	ES	$6s^{0.19}4f^{0.39}5d^{1.90}6p^{0.40}5f^{0.05}6d^{0.14}$	0.86

Table S15: Computed Ce^{3+} $4f^1$-$4f^1$ and $4f^1$-$5d^1$ Transition Energies (E), Transition Wavelengths (λ), and Oscillator Strengths (f) of $[Ce(H_2O)_9]^{3+}$ and $[Ce(H_2O)_8]^{3+}(H_2O)$ for geometries optimized at the PBE0 level of theory.

ectrum onal prism geometry, D_{3h} es (Å) 3 × 2.586; 6 × 2.565			emission spectrum **$[*Ce(H_2O)_9]^{3+}$** tricapped trigonal prism geometry, D_{3h} symmetry Ce-O distances (Å) 3 × 2.586; 6 × 2.565				emission spectrum **$[*Ce(H_2O)_8]^{3+}(H_2O)$** bicapped trigonal prismatic geometry, symmetry Ce-O mean distances (Å) 6×2.547, 2×1×4.328		
E, cm^{-1}	λ, nm	f, a.u.	transition	E, cm^{-1}	λ, nm	f, a.u.	transition	E, cm^{-1}	λ, nm
0			$4f^1$-$5d^1$	40255	249	0.0009	$4f^1$-$5d^1$	33451	299
127				40131	249	0.0015		33236	301
225				40034	250	0.0024		33097	302
2284				37971	263	0.0139		31126	321
2408				37850	264	0.0227		31028	322
2505				37752	265	0.0000		30940	323
2591				37667	266	0.0000		30629	327
40259	249	0.0000							
40739	246	0.0428							
42886	233	0.0023							
45820	218	0.0000							
46736	214	0.0008							

Table S16: Computed Ce^{3+} $4f^1$-$4f^1$ and $4f^1$-$5d^1$ Transition Energies (E), Transition Wavelengths (λ), and Oscillator Strengths (f) of $[Ce(H_2O)_7Cl_2]^+$ and $[Ce(H_2O)_6Cl_2]^+(H_2O)$ for geometries optimized at the PBE0 level of theory.

absorption spectrum $[Ce(H_2O)_7Cl_2]^+$ Ce-O distances (Å) 2 × 2.536; 3 × 2.579 ; 2 x 2.595 Ce-Cl distances (Å) 2 x 2.667				emission spectrum $[*Ce(H_2O)_6Cl_2],^+(H_2O)$ Ce-O distances (Å) 1 x 2.439 ; 4 × 2.497; 1 × 2.601 ; Ce-Cl distances (Å) 2 x 2.648			
transition	E, cm^{-1}	λ, nm	f, a.u.	transition	E, cm^{-1}	λ, nm	f, a.u.
$4f^1$-$4f^1$	0			$4f^1$-$5d^1$	26802	373	0.0174
	66				26330	380	0.0074
	289				26072	384	0.0002
	2270				24440	409	0.0152
	2342				24262	412	0.0048
	2484				23832	420	0.0000
	2656				23663	423	0.0001
$4f^1$-$5d^1$	38601	259	0.0170				
	38872	257	0.0179				
	42053	238	0.0096				
	42620	235	0.0028				
	45294	221	0.0007				

Table S17. Computed Ce^{3+} $4f^1$-$4f^1$ and $4f^1$-$5d^1$ transition energies $(in\ cm)^{-1}$ at the CASCSF level for $[Ce(H_2O)_9]^{3+}(H_2O)_{n=0,18}$ with (n = 18) and without (n = 0) explicit second hydration shell

	$[Ce(H_2O)_9]^{3+}$	$[Ce(H_2O)_9]^{3+}$	$[Ce(H_2O)_9]^{3+}(H_2O)_{18}$	$[Ce(H_2O)_9]^{3+}(H_2O)_{18}$
	gas-phase	PCM	gas-phase	PCM
$4f^1$-$4f^1$	0	0	0	0
	290	227	207	215
	461	425	422	426
	464	432	425	429
	497	441	430	437
	497	449	430	439
	703	696	696	695
$4f^1$-$5d^1$	42495	42247	42139	42120
	44809	44898	44937	44924
	44909	45018	45036	45021
	47383	47233	47231	47224
	47405	47266	47254	47239

Table S18. Computed Ce^{3+} $4f^1$-$4f^1$ and $4f^1$-$5d^1$ spin-free Transition Energies (*E*) for $[Ce(H_2O)_9]^{3+}$ at the MS-CASPT2 and TD-DFT levels using PBE0 functional with PCM non Eq.

	MS-CASPT2	TD-DFT PBE0
$4f^1$-$4f^1$	42	2348
	53	2361
	74	2479
	233	4872
	365	5251
	417	5260
$4f^1$-$5d^1$	40472	42308
	41483	43465
	41501	43632
	45355	47308
	45375	47344

3. References

(1) (a) Albertsson, J.; Elding, L. I. The Geometry of the Nonaaqualanthanoid(3+) Complex in the Solid Bromates and Ethyl Sulphates. *Acta Crystallogr. B* **1979**, *33*, 1460-1469. (b) Abbasi, A.; Lindqvist-Reis, P.; Eriksson, L.; Sandström, D.; Lidin, S.; Persson, I.; Sandström, M. Highly Hydrated Cations: Deficiency, Mobility, and Coordination of Water in Crystalline Nonahydrated Scandium(III), Yttrium(III), and Lanthanoid(III) Trifluoromethanesulfonates. *Chem. Eur. J.* **2005**, *11*, 4065–4077. (c) Habenschuss, A.; Spedding, F. H. di-μ-chloro-bis[heptaaqualanthanum(III)] tetrachloride $[(H_2O)_7La_2(H_2O)_7]CL_4$ *Cryst. Struct. Commun*. **1979**, *8*, 511–516. (d) Rogers, R. D.; Kurihara, L. K. f-Element/Crown Ether Complexes. 1. Synthesis and structure of $[Y(OH_2)_8]Cl_3 \cdot$(15-crown-5). *Inorg. Chim. Acta* **1986**, 116, 171–177. (e) Bell, A, M. T.; Smith, A. J. *Acta Crystallogr. C* **1990**, *46*, 960–962.

(2) *CrysAlis PRO*, Agilent Technologies, Version 1.171.36.20 (Release 27-06-2012 CrysAlis171 .NET) (compiled Jul 11 2012,15:38:31); Program(s) Used to Refine Structure: *SHELXL2018*/1 (Sheldrick, 2018).

(3) Adamo, C.; Barone. V. Toward Reliable Density Functional Methods without Adjustable Parameters: The PBE0 Model *J. Chem. Phys.* **1999**, *110*, 6158-6169.

(4) Furche, F.; Ahlrichs. R. Adiabatic Time-Dependent Density Functional Methods for Excited State Properties. Chem. Phys. **2002**, *117*, 74337447.

(5) Hättig, C.; Hellweg, A.; Köhn, A. Distributed Memory Parallel Implementation of Energies and Gradients for Second-Order Møller–Plesset Perturbation Theory with the Resolution-of-the-Identity Approximation. *Phys. Chem. Chem. Phys.* **2006**, *8*, 1159-1169; b) Hättig, C.; Weigend, F. CC2 Excitation Energy Calculations on Large Molecules Using the Resolution of the Identity Approximation. *J. Chem. Phys.* **2000**, *113*, 5154-5161.

(6) Weigend, F.; Köhn, A.; Hättig, C. Efficient Use of the Correlation Consistent Basis Sets in Resolution of the Identity MP2 Calculations. *J. Chem. Phys.* **2002**, *116*, 3175-3183.

(7) Hättig, C. Optimization of Auxiliary Basis Sets for RI-MP2 and RI-CC2 Calculations: Core–Valence and Quintuple-ζ Basis Sets for H to Ar and QZVPP Basis Sets for Li to Kr. *Phys. Chem. Chem. Phys.* **2005**, *7*, 59-66.

(8) Andersson, K.; Malmqvist, P.-Å.; Roos, B. O.; Sadlej, A. J.; Wolinski, K. Second-Order Perturbation Theory with a CASSCF Reference Function. *J. Phys. Chem.*, **1990**, *94*, 5483.

(9) Andersson, K.; Malmqvist P.-Å., Roos, B. O. Second-Order Perturbation Theory with a Complete Active Space Self-Consistent Field Reference Function. *J. Chem. Phys.*, **1992**, *96*, 1218.

(10) Finley, J.; Malmqvist, P.-Å.; Roos B. O. Serrano-Andrés, L. The Multi-State CASPT2 Method. *Chem. Phys. Lett.*, **1998**, *288*, 299-306.

(11) Dolg, M.; Stoll, H.; Preuss, H. Energy-Adjusted Ab Initio Pseudopotentials for the Rare Earth Elements. *J. Chem. Phys*. **1989**, *90*, 1730.

(12) Cao, X.; Dolg, M. Segmented Contraction Scheme for Small-core Lanthanide Pseudopotential Basis Sets. *J. Mol. Struct. Theochem*. **2002**, *581*, 139-147.

(13) Woon, D.E.; Dunning, T.H. Jr. Gaussian Basis Sets for Use in Correlated Molecular Calculations. IV. Calculation of Static Electrical Response Properties. *J. Chem. Phys.* **1994**, *100*, 2975.

(14) Dunning, T.H. Jr. Gaussian Basis Sets for Use in Correlated Molecular Calculations. I. The Atoms Boron Through Neon and Hydrogen. *J. Chem. Phys.* **1989**, *90*, 1007.

(15) TURBOMOLE V7.1 2016, a development of University of Karlsruhe and Forschungszentrum Karlsruhe GmbH, 1989-2007, TURBOMOLE GmbH, since 2007; available from http://www.turbomole.com.

(16) Douglas M.; Kroll, N. M. *Ann. Phys*., **1974**, *82*, 89; Hess, B. A. Relativistic Electronic-Structure Calculations Employing a Two-Component No-Pair Formalism with External-Field Projection Operators. *Phys. Rev. A* **1986**, *33*, 3742.

(17) Ghido, G.; Roos, B. O.; Malmqvist, P.-Å. A Modified Definition of the Zeroth-Order Hamiltonian in Multiconfigurational Perturbation Theory (CASPT2). *Chem. Phys. Lett*. **2004**, *396*, 142-149.

(18) Målmqvist, P.-A.; Roos, B. O.; Schimmelpfennig, B. The Restricted Active Space (RAS) State Interaction Approach with Spin-Orbit Coupling. *Chem. Phys. Lett*. **2002**, *357*, 230-240.

(19) Heß, B. A.; Marian, C. M.; Wahlgren, U.; Gropen, O. A mean-field spin-orbit method applicable to correlated wavefunctions. *Chem. Phys. Lett*. **1996**, *251*, 365-371.

(20) Schimmelpfennig, B. AMFI, an Atomic Mean-Field Integral Program.

(21) Aquilante, F.; Autschbach, J.; Carlson, R. K.; Chibotaru, L. F.; Delcey, M. G.; De Vico, L.; Fdez Galván, I.; Ferré, N.; Frutos, L. M.; Gagliardi, L.; Garavelli, M.; Giussani, A.; Hoyer, C. E.; Li Manni, G.; Lischka, H.; Ma, D.; Malmqvist, P.-A.; Müller, T.; Nenov, A.; Olivucci, M.; Pedersen, T. B.; Peng, D.; Plasser, F.; Pritchard, B.; Reiher, M.; Rivalta, I.; Schapiro, I.; Segarra-Mart, J.; Stenrup, M.; Truhlar, D. G.; Ungur, L.; Valentini, A.; Vancoillie, S.; Veryazov, V.; Vysotskiy, V. P.; Weingart, O.; Zapata, F.; Lindh, R. Molcas 8: New Capabilities for Multiconfigurational Quantum Chemical Calculations Across the Periodic Table. *J. Comput. Chem*. **2016**, *37*, 506.

(22) Barone V.; Cossi. M. Quantum Calculation of Molecular Energies and Energy Gradients in Solution by a Conductor Solvent Model *J. Phys. Chem. A* **1998**, *102*, 1995-2001.

(23) Cossi, M.; Rega, N.; Scalmani, G.; Barone. V. Polarizable dielectric model of solvation with inclusion of charge penetration effects. J. Chem. Phys. **2001**, *114*. 5691.

(24) Gaussian 09, Revision E.01, M. J. Frisch, G. W. Trucks, H. B. Schlegel, G. E. Scuseria, M. A. Robb, J. R. Cheeseman, G. Scalmani, V. Barone, G. A. Petersson, H. Nakatsuji, X. Li, M. Caricato, A. Marenich, J. Bloino, B. G. Janesko, R. Gomperts, B. Mennucci, H. P. Hratchian, J. V. Ortiz, A. F. Izmaylov, J. L. Sonnenberg, D. Williams-Young, F. Ding, F. Lipparini, F. Egidi, J. Goings, B. Peng, A. Petrone, T. Henderson, D. Ranasinghe, V. G. Zakrzewski, J. Gao, N. Rega, G. Zheng, W. Liang, M. Hada, M. Ehara, K. Toyota, R. Fukuda, J. Hasegawa, M. Ishida, T. Nakajima, Y. Honda, O. Kitao, H. Nakai, T. Vreven, K. Throssell, J. A. Montgomery, Jr., J. E. Peralta, F. Ogliaro, M. Bearpark, J. J. Heyd, E. Brothers, K.

N. Kudin, V. N. Staroverov, T. Keith, R. Kobayashi, J. Normand, K. Raghavachari, A. Rendell, J. C. Burant, S. S. Iyengar, J. Tomasi, M. Cossi, J. M. Millam, M. Klene, C. Adamo, R. Cammi, J. W. Ochterski, R. L. Martin, K. Morokuma, O. Farkas, J. B. Foresman, and D. J. Fox, Gaussian, Inc., Wallingford CT, 2016.

(25) AIMAll (Version 12.06.21), Todd A. Keith, TK Gristmill Software, Overland Park KS, USA, 2012 (aim.tkgristmill.com).

(26) Miyakawa, K.; Kaizu, Y.; Kobayashi, H. An Electrostatic Approach to the Structure of Hydrated Lanthanoid Ions. $[M(OH_2)_9]^{3+}$ versus $[M(OH_2)_8]^{3+}$. *J. Chem. Soc. Faraday Trans. 1* **1988**, *84*, 1517-1529.

(27) Lindqvist-Reis, P.; Klenze, R.; Schubert, G.; Fanghänel, T. Hydration of Cm^{3+} in Aqueous Solution from 20 to 200 °C. A Time-Resolved Laser Fluorescence Spectroscopy Study *J. Phys. Chem. B* **2005**, *109*, 3077-3083.